JOURNAL OF PROPULSION AND POWER
Vol. 25, No. 3, May–June 2009

Computational Analysis of the Oxidizer Preflow in an Upper-Stage Rocket Engine

Roland Schmehl* and Johan Steelant†
ESA, 2200 AG Noordwijk, The Netherlands

DOI: 10.2514/1.38309

A detailed computational analysis of the oxidizer preflow during startup of a storable propellant upper-stage rocket engine is presented. This low-pressure flow regime is controlled by various two-phase phenomena, particularly flash atomization and flash evaporation of superheated liquid oxidizer, leading to a significant temperature drop in the combustion chamber. To account for these phenomena, physical models are extended to low-pressure conditions and implemented into the framework of an iterative Euler–Lagrange method. A new semi-implicit concept of the spray source term linearization is employed, improving the robustness of the numerical solution procedure by accounting for intense coupling of vapor flow and spray. Following the analysis of the three-dimensional two-phase flowfield and spray deposit distribution in the combustion chamber and nozzle extension, the influence of liquid injection temperature and initial droplet size distribution is investigated by detailed parametric studies. The results indicate a particular importance of the spray–wall interaction and secondary-droplet breakup for the coarser sprays and a bimodal deposit distribution on the chamber walls. Computational results agree well with experimental data and are used to derive transfer functions describing global preflow dynamics on a system level.

Nomenclature

B_T	=	heat transfer number
c	=	absolute velocity, m/s
c_D	=	aerodynamic drag coefficient
c_p	=	specific heat at constant pressure, J/kg/K
D	=	droplet diameter, μm
D_{32}	=	Sauter mean diameter, μm
D_{63}	=	Rosin–Rammler mean diameter, μm
f	=	droplet number rate, 1/s
h	=	specific enthalpy, J/kg
H	=	enthalpy, J
k	=	turbulent kinetic energy, m^2/s^2
La	=	Laplace number
M	=	Mach number
m	=	mass, kg
$\dot{m}$	=	mass flux, kg/s
Nu	=	Nusselt number
n	=	Rosin–Rammler width parameter
Pr	=	Prandtl number
p	=	pressure, Pa
$\dot{Q}$	=	energy flux, J/s
R	=	residual
Re	=	Reynolds number
r	=	droplet radial coordinate, m
S	=	splashing parameter
S_ϕ	=	source term
s^w_{md}	=	liquid deposition density, $kg/m^2/s$
T	=	temperature, K
t	=	time, s
u, v, w	=	Cartesian velocity components, m/s
We	=	Weber number
α_s	=	heat transfer coefficient, $W/m^2/K$
Δt	=	residence time, s
Δh_v	=	specific enthalpy of vaporization, J/kg
ε	=	dissipation rate of k, m^2/s^3
γ	=	under-relaxation factor
λ	=	thermal conductivity, W/m/K
μ	=	dynamic viscosity, Pa · s
ν	=	deposit mass fraction
ρ	=	density, kg/m^3
ϕ	=	flow variable
σ	=	surface tension, N/m

Subscripts

b	=	boiling state
d	=	droplet
dep	=	deposition
f	=	flashing
g	=	gaseous
i	=	droplet interior to surface
inj	=	injection
k	=	trajectory index
L	=	Leidenfrost
l	=	liquid
n	=	surface normal
ref	=	reference state
rel	=	relative
s	=	droplet surface
stat	=	steady state
vap	=	vapor
w	=	wall
0	=	initial state, equilibrium state
∞	=	droplet far-field state

Received 29 April 2008; revision received 19 December 2008; accepted for publication 11 January 2009.

*European Space Research and Technology Centre, Propulsion and Aerothermodynamics Division; currently Software Architect, TNO Automotive Safety Solutions; roland.schmehl@tass-safe.com.

†Senior Research Engineer, European Space Research and Technology Centre, Propulsion and Aerothermodynamics Division; johan.steelant@esa.int. Member AIAA.

I. Introduction

THE startup of a storable propellant upper-stage rocket engine typically involves a short oxidizer preflow phase before the injection of the liquid fuel. This oxidizer lead configuration ensures that the hypergolic propellants get in contact at a well-defined minimum pressure, avoiding excessive ignition delays and propellant accumulation and thus decreasing the risk of startup

anomalies [1,2]. In the absence of combustion, the pressure and temperature levels in the preflow phase are predominantly controlled by the evaporation rate of the liquid oxidizer and are far below the respective levels at nominal operation of the engine. Because of the severe pressure drop from oxidizer dome to combustion chamber, the injected liquid is in a superheated thermodynamical state. As a consequence, spontaneous vapor formation and expansion within the liquid leads to flash atomization, a mechanism that is characterized by extended spray cones and significantly reduced droplet sizes. Accordingly, heat and mass transfer from the spray to the vapor flow is governed by flash evaporation. In contrast to conventional droplet evaporation, this evaporation mechanism is controlled by the transfer of energy from the droplet interior to its surface.

Because of the limited energy content and the absence of other energy sources and, to a lesser extent, due to the finite rate phase change and the short residence time in the chamber, only a fraction of the injected liquid actually evaporates in the combustion chamber during preflow. A considerable fraction of the spray deposits on the chamber walls, undergoing further flash evaporation and film transport. These processes depend on the degree of superheat of the deposit, the thermal state of the wall, the shear stress on the liquid–vapor interface, and volume forces such as gravity or thrust. In the expanding nozzle flow, the spray is accelerated and exposed to a steep drop of pressure and temperature. In this region, the two-phase mixture is again characterized by intense flash evaporation of the spray droplets.

The phase transition from pressurized stored liquid to dispersed two-phase mixture in the combustion chamber and expansion nozzle is illustrated in Fig. 1 for the oxidizer N_2O_4 used in the present analysis. Following the nearly isobaric flash evaporation at the chamber pressure p_{stat}, the thermodynamic nonequilibrium character of the two-phase flow is further pronounced in the expansion nozzle. This is indicated by the phase trajectory of subcooled vapor proceeding from the equilibrium boiling state into the solid region and that of a superheated flash-evaporating 50 μm droplet in the gaseous region of the phase diagram.

The presented analysis has been conducted in the frame of a comprehensive system-level investigation of upper-stage engine startup behavior and has been motivated by the need for increased reliability of multiple engine firings during complex mission scenarios [3–7]. A major objective is the refined understanding and modeling of the low-pressure two-phase flow dynamics in the combustion chamber to provide an accurate system-level model of the preflow that is capable of identifying potential causes of ignition delay and combustion instabilities. The paper expands on previous contributions [8,9] proposing a new semi-implicit treatment of the spray source terms for high interphase transfer rates and a consistent adaptation of the modeling framework to account for the superheated state of the injected liquid propellant. Thus, a particular focus is on the processes of flash atomization and flash evaporation of droplets and liquid wall deposit. Deformation and breakup of droplets by aerodynamic forces and droplet wall impact are covered by empirical models originally developed to describe fuel preparation in lean-premixed prevaporized (LPP) combustors [10–13]. Computational results are presented for the Aestus upper-stage engine, which is employed in the base configuration of the European launcher Ariane 5. Following a detailed analysis and discussion of the two-phase flowfield and wall-deposit distribution, the influence of the spray initial conditions and wall conditions is evaluated by means of a comprehensive parametric study. Transfer functions are derived to describe the dynamic evolution of the vapor flowfield and the influence of initial and boundary conditions on a system-analysis level.

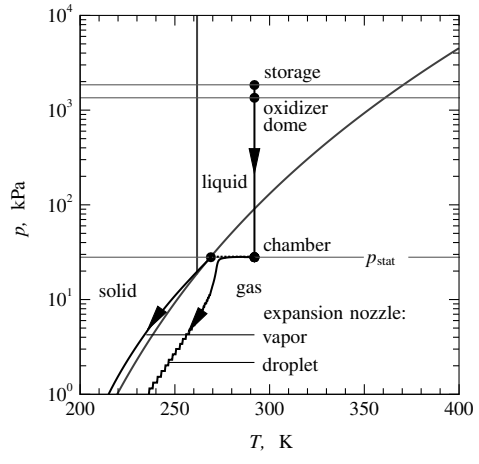

Fig. 1 Thermodynamic phase transition of N_2O_4.

II. Computational Method

Mathematical models of dispersed two-phase flows can be classified into two conceptual approaches [13]. In the Euler–Euler approach, the gas phase and the dispersed liquid phase are described as interpenetrating and interacting continua, whereas in the Euler–Lagrange approach, the dispersed phase is regarded as a superposition of individual droplet trajectories. Euler–Euler methods are generally well-suited for strongly coupled two-phase flows, because the discretized transport equations for gas and dispersed liquid phases are solved simultaneously, accounting for interphase transfer of mass, momentum, and energy [14]. However, to accurately represent sprays that are characterized by droplets of widely varying size and initial velocities, many separate phase continua may be required and, as consequence, the computational effort can increase substantially with the complexity of the spray. On the other hand, the different mathematical models and solution procedures employed in Euler–Lagrange methods introduce an artificial numerical phase decoupling, which can lead to stability problems in the iterative solution process, especially for high interphase transfer rates. Yet, the major advantage of these methods is the accurate representation of complex polydisperse two-phase flows involving liquid atomization, secondary breakup, and wall interaction effects [15,16]. To combine the advantages of both concepts, hybrid methods have been proposed [17]. The presented analysis employs the computational fluid dynamics package METIS-Ladrop, which has been developed at the Institute for Thermal Turbomachinery of the University of Karlsruhe on the basis of an Euler–Lagrange approach.

A. Iterative Euler–Lagrange Method

With liquid volume concentrations of around 1%, the oxidizer preflow in most parts of the combustion chamber can be regarded as a *dilute* two-phase flow in which the droplet motion is controlled by local aerodynamic forces [13,18]. Exceptions are the atomization regions in the immediate vicinity of the propellant injectors, in which the concentration approaches values that are characteristic of *dense* two-phase flow and the effect of droplet collisions may not be neglected anymore. In the present analysis, it is assumed that dense-spray effects are covered implicitly by the empirical atomization model. As a consequence, interaction between droplets is not considered explicitly in the trajectory model, which reduces the computational complexity substantially.

Furthermore, the volume fraction of the liquid phase is not taken into account in the transport equations of the continuous phase, thus limiting the effect of the spray on the vapor flow exclusively to the spray source terms. At typical steady-state preflow conditions with $p_{stat} \approx 30$ kPa and $T_{stat} \approx 290$ K, around 10% of the N_2O_4 molecules are dissociated into NO_2 [2]. Because of its short time scale, this chemical reaction can be regarded as instantaneous. In the present analysis, it is taken into account in the pressure- and temperature-dependent correlations for thermophysical properties.

The basic setup of an Euler–Lagrange coupling cycle is illustrated in Fig. 2. The vapor flow is described by the Reynolds-averaged Navier–Stokes (RANS) equations combined with a standard k-ε turbulence closure model. To cover the evolution from low-subsonic flow ($M \approx 0.1$) in the combustion chamber to supersonic flow ($M \approx 2$) at the outflow boundary, a compressible formulation of the SIMPLEC pressure-correction scheme is employed to represent the

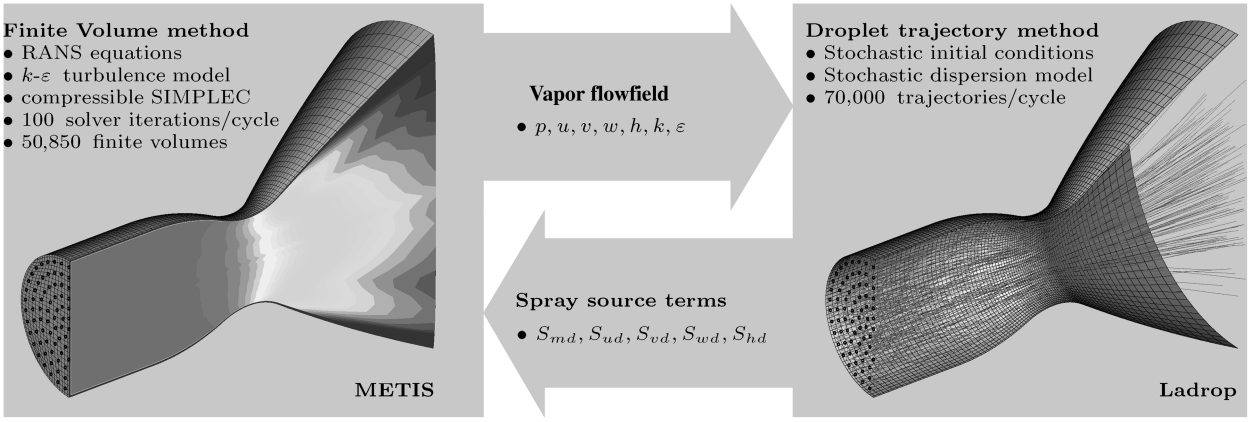

Fig. 2 Main features of the iterative Euler–Lagrange method implemented in METIS-Ladrop.

coupled pressure-velocity field [19]. The computational domain, a 180 deg section of the flow domain, is discretized by a contour-fitted $113 \times 30 \times 15$ finite volume mesh. The convective terms of the momentum and enthalpy equations, as well as the density at the faces of the discretization volumes, are approximated by the second-order-accurate monotonized-linear-upwind (MLU) scheme [20]. For stability reasons, the convective terms of the pressure correction and turbulence transport equations are approximated by an upwind scheme. The final set of equations is cast into the general form

$$a_P^{\phi}\phi_P = \sum_{nb} a_{nb}^{\phi}\phi_{nb} + S_{\phi}^{C} + S_{\phi d}, \qquad \phi = p', u, v, w, h, k, \varepsilon \quad (1)$$

describing the linearized relationship between flow variables of central volume P and neighboring volumes nb. The constant part S_{ϕ}^{C} of the general source term includes higher-order terms, whereas the spray source term $S_{\phi d}$ is computed as a statistical average of droplet trajectory data according to

$$S_{p'd} \equiv S_{md} = \sum_{k=1}^{N} f_k (m_d^{in} - m_d^{out})_k \quad (2)$$

$$S_{\phi d} = \sum_{k=1}^{N} f_k (m_d^{\text{in}}\phi_d^{\text{in}} - m_d^{\text{out}}\phi_d^{\text{out}})_k, \qquad \phi = u, v, w, h \quad (3)$$

Droplet mass, momentum, and enthalpy on trajectory k are evaluated on entry (in) and exit (out) of the discretization volumes [21]. Preliminary investigations showed that the effect of the spray source terms on the transport equations of k and ε is insignificant and, consequently, a modulation of turbulence is not considered in the present analysis. The central coefficients in Eqs. (1) are evaluated as

$$a_P^{p'} = \sum_{nb} a_{nb}^{p'} \quad (4)$$

$$a_P^{\phi} = \sum_{nb} a_{nb}^{\phi} - S_{\phi}^{P} + S_{md}, \qquad \phi = u, v, w, h \quad (5)$$

where S_{ϕ}^{P} represents the proportional part of the general source term and S_{md} represents an additional closing term as a result of interphase mass transfer. The resulting system of linearized equations is solved block-iteratively using a Bi-CGSTAB algorithm method with standard incomplete lower/upper (ILU) preconditioning.

The droplet motion in the vapor flow is described by a modified Basset–Boussinesq–Oseen equation assuming locally uniform flow, neglecting the effects of added mass, Basset history, and unsteady force terms and retaining only the steady-state drag term, as is generally applicable for spray combustion processes [18,22]:

$$m_d \frac{d\boldsymbol{u}_d}{dt} = -\frac{\pi}{8} D^2 \rho c_D c_{\text{rel}} (\boldsymbol{u}_d - \boldsymbol{u}) \quad (6)$$

The effect of droplet deformation on the aerodynamic drag is accounted for by an empirical correlation [23,24]:

$$c_D = 0.28 + \frac{21}{Re} + \frac{6}{\sqrt{Re}} + We(0.2319 - 0.1579 \log Re + 0.047 \log^2 Re - 0.0042 \log^3 Re) \quad (7)$$

which is valid in the range of $5 \leq Re \leq 4000$, with Reynolds and Weber numbers defined as

$$Re = \frac{\rho c_{\text{rel}} D}{\mu}, \qquad We = \frac{\rho c_{\text{rel}}^2 D}{\sigma} \quad (8)$$

Equation (6) is integrated numerically using a Runge–Kutta–Fehlberg (RKF45) method with adaptive step-size control. Droplet initial conditions are generated on the basis of an empirical model describing the flash atomization of superheated liquid propellant from a plain-orifice injector. The procedure employing random distributions for injection angle and droplet size is described in detail in Sec. II.C. The droplet flash evaporation model is elaborated in Sec. II.D. The effect of flow turbulence on spray dispersion is simulated by velocity fluctuations that are generated stochastically along the trajectories, according to local turbulence properties [25]. The wall impact of droplets is governed by a detailed set of interaction mechanisms, including deposition, splashing, nucleate boiling, film boiling, and reflection.

The theoretical framework has been employed in previous studies [10] and is adapted to superheated liquid in Sec. II.E. Droplet deformation and breakup by aerodynamic forces is accounted for by empirical correlations describing classification, temporal and spatial evolution, and secondary-fragment size spectra of various mechanisms [10–12]. Although homogeneous condensation and ice formation occur for certain operation modes of the engine, these phenomena are not considered, because they affect only the flow past the throat, which exhibits a strong pressure drop.

The dispersed-phase flowfield is evaluated as a superposition of trajectory data on the finite volume mesh [21]. Consequently, the level of detail and the statistical quality of the resulting field data improve with the number of computational droplets employed, each representing a collection of physical droplets with similar initial conditions. For optimal convergence of the Euler–Lagrange coupling iterations and to achieve a required accuracy of the computed two-phase flowfield, it is important to adjust the statistical quality of the spray source terms to the computational accuracy of the finite volume solver. The iterative procedure requiring semi-implicit treatment and under-relaxation of the spray source terms is detailed in the following section.

B. Semi-Implicit Treatment of Spray Source Terms

Because the vapor flow is generated entirely by evaporating liquid, the spray source term is a dominant contribution in the transport equations. Applying $S_{\phi d}$ directly to the right-hand side of Eq. (1)

generally causes the numerical solution process to become unstable. To increase the diagonal dominance of the system matrix, the source term is decomposed into a proportional and a constant part

$$S_{\phi d} = S^P_{\phi d}\phi + S^C_{\phi d} \tag{9}$$

performing the following operations [26]:

1) For $S^P_{\phi d} < 0$, subtract $S^P_{\phi d}$ from a^ϕ_P and add $S^C_{\phi d}$ to the right-hand side of Eq. (1) (implicit treatment).

2) For $S^P_{\phi d} > 0$, add the full source term $S_{\phi d}$ to the right-hand side of Eq. (1) (explicit treatment).

This formal decomposition can be regarded as a linearization of the functional dependency $S_{\phi d}(\phi)$ in the vicinity of the current solution value ϕ^i, with the effectiveness of the approach depending on how well $S^P_{\phi d}$ approximates the derivative $[\partial S_{\phi d}/\partial\phi]^i$. The present analysis employs the concept of a zero-source state ϕ_0 representing a virtual variation of the transport variable at which the source term locally disappears [27]. The resulting linear approximation is illustrated in Fig. 3 and defined by

$$S^P_{\phi d} = \frac{S^i_{\phi d}}{\phi^i - \phi_0}, \qquad S^C_{\phi d} = -\frac{S^i_{\phi d}\phi_0}{\phi^i - \phi_0} \tag{10}$$

For the spray source term to disappear, the two-phase flow has to be in mechanical and thermal equilibrium. In this state, the gas-phase velocity and temperature adopt the values of the dispersed phase:

$$p'_0 = 0 \tag{11}$$

$$u_0 = \bar{u}_d, \qquad v_0 = \bar{v}_d, \qquad w_0 = \bar{w}_d, \qquad h_0 = h(\bar{T}_d) \tag{12}$$

The Eulerian mean values of the dispersed phase are defined as statistical mass averages according to

$$\bar{\phi}_d = \frac{\sum_{k=1}^N f_k \Delta t_k (\overline{m_d \phi_d})_k}{\sum_{k=1}^N f_k \Delta t_k (\bar{m}_d)_k}, \qquad \phi = u, v, w, h \tag{13}$$

and the temperature $\bar{T}_d$ is computed from the mean enthalpy $\bar{h}_d$ by an iterative Newton method. The droplet residence time per discretization volume and the associated mean values are evaluated as

$$\Delta t_k = (t^{\text{out}} - t^{\text{in}})k \tag{14}$$

$$(\bar{m}_d)_k = \tfrac{1}{2}(m^{\text{in}}_d + m^{\text{out}}_d)_k \tag{15}$$

$$(\overline{m_d\phi_d})_k = \tfrac{1}{2}(m^{\text{in}}_d\phi^{\text{in}}_d + m^{\text{out}}_d\phi^{\text{out}}_d)_k, \qquad \phi = u, v, w, h \tag{16}$$

To account for the variation of ϕ^i along the subiterations of the linear equation solver, the source-term decomposition has to be continuously updated to ensure that the total effective value $S^i_{\phi d}$ stays constant throughout each Euler–Lagrange coupling cycle. Test computations have indicated that instead of adapting $S^P_{\phi d}$ and $S^C_{\phi d}$ according to Eq. (10), the robustness is improved by keeping $S^P_{\phi d}$ constant for each coupling cycle while adapting only the constant part of the source term:

$$S^C_{\phi d} = S^i_{\phi d} - S^P_{\phi d}\phi^i \tag{17}$$

Additionally, the computed spray source terms need to be damped by under-relaxation to avoid instability of the numerical solution due to the strong coupling of vapor flow and spray:

$$S^{i+1}_{\phi d} = \gamma S^{i*}_{\phi d} + (1-\gamma)S^i_{\phi d} \tag{18}$$

In this formulation, $S^i_{\phi d}$ and $S^{i+1}_{\phi d}$ denote the source terms that are effective in the transport equations of the current and the next Euler–Lagrange coupling cycle, respectively, and $S^{i*}_{\phi d}$ denotes the source term computed by the trajectory method in the current cycle. Using a relaxation factor of $\gamma = 3\%$, which is the maximum stable value for the present flow problem, a large number of coupling iterations are necessary to include 100% of the spray sources in the vapor flow computation. This is demonstrated in Table 1, specifying the ratio of effective and computed source terms, starting from $S^1_{\phi d} = 0$ and assuming that $S^{i*}_{\phi d} = \text{const}$.

Table 1 Under-relaxation with $\gamma = 3\%$

Iteration i	$S^i_{\phi d}/S^{i*}_{\phi d}$, %
1	0
100	95.098
200	99.767
300	99.989
400	99.999

Thus, in the present analysis, 400 Euler–Lagrange coupling cycles are performed in the first stage of the simulation to ramp up and stabilize the interaction of continuous and particulate phases. Because accuracy is not of highest priority at this stage, each cycle consists of 100 iterations of the linear equation solver, followed by an integration of 70,000 primary droplet trajectories and an additional 210,000 trajectories of droplets from secondary-droplet breakup events and droplet splashing at the chamber wall. In the second stage, 95 Euler–Lagrange coupling cycles are performed, with the number of primary trajectories increased to 700,000 per cycle to improve the statistical quality of the spray source term distribution. In the final stage, the linear equation solver operates on a frozen distribution of the spray source terms until the residual norm is decreased by 4 orders of magnitude. This is generally achieved within 2000 iterations, as illustrated in Fig. 4, showing the evolution of the pressure-correction residual toward the end of the Euler–Lagrange coupling iterations.

Because the spray source term acts as a perturbation term in the RANS equations, the residual at the begin of each coupling iteration exhibits a characteristic jump that depends on the degree of interphase coupling [28]. Another contributing factor is the statistical noise in the spray source term field, which can be significant even when a very large number of trajectories are employed. The total simulation time is approximately 20 CPU days on a standard 3-GHz

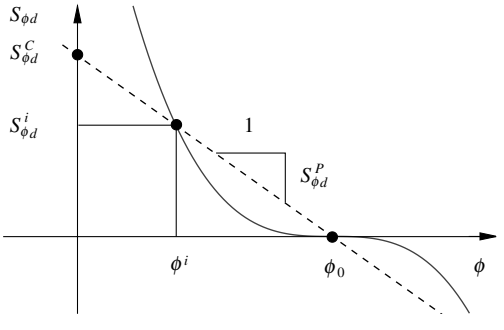

Fig. 3 Spray source term linearization.

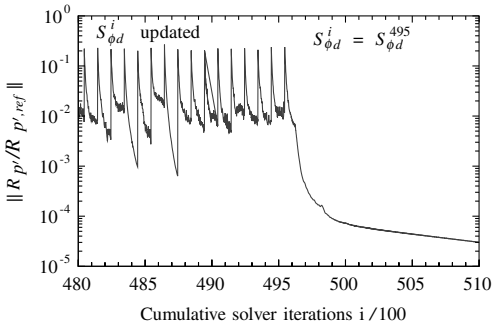

Fig. 4 Residual of the pressure-correction equation.

Pentium 4 PC. Starting from an existing flowfield, a solution for modified problem parameters is reached in 10 CPU days.

The described solution procedure has been developed on the basis of previous research on two-phase flows in combustion engines [10,14,16,17,29]. The mesh resolution and particle numbers employed are the final result of a convergence analysis, which indicated that further refinement resulted in only minor local variations of the flowfields and did not influence the results of interest, such as chamber temperature, pressure level, and spray deposition density.

C. Empirical Flash Atomization Model

During preflow, the coaxial injector elements operate as plain-orifice injectors in a flash atomization mode. Compared with classical jet breakup, this mode is characterized by rapid internal vapor formation, resulting in a burstlike expansion of the jet upon entering the low-pressure environment of the combustion chamber. Experimental visualizations, as shown in Fig. 5 (left), indicate spray cone angles of about $\theta_{\max} = 50$ deg for typical preflow conditions [30]. The computational model of the flash atomization process is depicted in Fig. 5 (right) by representative droplet trajectories.

Droplet initial conditions are generated from suitable random distributions reproducing the solid cone structure of the oxidizer spray. The offaxis angle is derived from a clipped normal distribution with mean value $\mu = 0$ deg, variance $\sigma = 45$ deg, and maximum $\theta_{\max} = 50$ deg. In this way, droplet density is high on the injector axis and decreases toward the outer region of the spray. The constant value of the droplet velocity $c_{d,0} = 20$ m/s is derived from the jet exit velocity. Because of the destructive effect of vapor pressure forces, droplet sizes are significantly reduced. Detailed analyses of sprays with similar visual appearance, degrees of superheat, and pressure drop indicate that droplet diameters hardly exceed 100 μm, whereas Sauter mean diameters range from 10 up to 50 μm [31,32].

Recent measurements of droplet sizes from plain-orifice atomizers at low-pressure preflow conditions have confirmed this [33]. Because of the uncertainties in the few available experimental data for low-pressure flow conditions, the influence of initial droplet size spectra is investigated by a parametric study. Assuming a Rosin–Rammler size distribution [34,35] with a fixed width parameter $n = 2.4$, this study covers size spectra with diameter parameters ranging from 50 up to 150 μm in steps of 10 μm for a constant injection temperature of $T_{d,0} = 292$ K. Three representative size spectra are illustrated in Fig. 6.

A second parametric study addresses the influence of injection temperature on preflow behavior. For a fixed droplet mean diameter $D_{63,0} = 100$ μm, this study covers a temperature range from 274 K, which is close to the triple point of the oxidizer, up to 300 K in steps of 2 K. In a final step, the injector matrix on the base plate of the combustion chamber is reconstructed based on this single-injector model. The specific injector arrangement on the base plate used in the present analysis is shown in the right part of Fig. 2.

D. Droplet Flash Evaporation Model

An essential component of the present study is an extension of classical D^2 theory [36] to flash evaporation of superheated droplets.

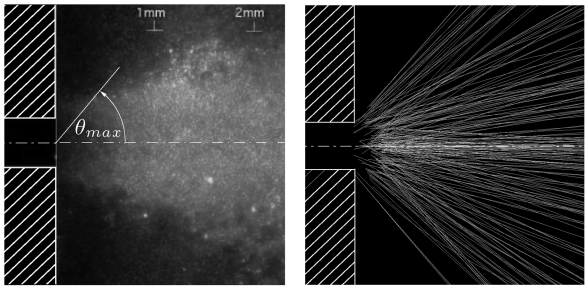

Fig. 5 Flash atomization from a single injector (image from [30]).

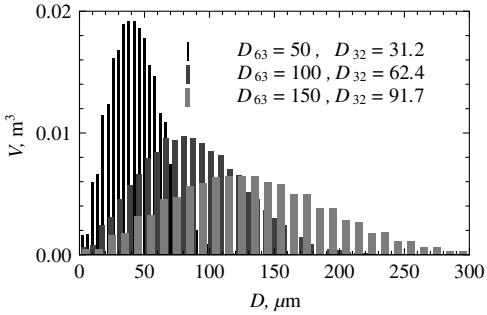

Fig. 6 Initial droplet size distribution.

The analytical framework is based on the assumption of spherically symmetric quasi-steady transport in the vapor phase around the droplet and a uniform temperature within the droplet. In this idealization, the net energy flux and vapor mass flux leaving the droplet are independent of the radial position. Both fluxes are interlinked by the differential energy balance in the vapor phase

$$\dot{Q} = \dot{m}_{\text{vap}} h(T) - 4\pi r^2 \lambda \frac{dT}{dr}, \qquad r_s < r < \infty \tag{19}$$

and the integral energy and mass balances of the droplet:

$$\frac{dH_d}{dt} = m_d c_{p,l} \frac{dT_d}{dt} - \dot{m}_{\text{vap}} h_l(T_d) = -\dot{Q} \tag{20}$$

$$\frac{dm_d}{dt} = -\dot{m}_{\text{vap}} \tag{21}$$

where the droplet enthalpy is given as $H_d = m_d h_l(T_d)$. Classical D^2 theory applies to a cold droplet ($T_d < T_b$) exposed to a hot vapor ($T_\infty > T_b$) and divides the droplet lifetime into a heat-up phase ($dT_d/dt > 0$ and $\dot{m}_{\text{vap}} = 0$) and an isothermal evaporation phase ($dT_d/dt = 0$ and $\dot{m}_{\text{vap}} > 0$). Consequently, Eq. (19) can be integrated along the radial coordinate, leading to closed analytical solutions for the heat-up and evaporation phases.

If the droplet is superheated, the surface temperature adapts immediately to the boiling temperature at the ambient pressure, and the evaporation process is controlled mainly by the energy transfer from the droplet interior to its surface. For low degrees of superheat, heat conduction and convection are the predominant transfer processes within the liquid. For higher degrees of superheat, the energy transfer is drastically intensified by nucleation of vapor bubbles. Because of the complexity of these phenomena, the internal energy transfer is modeled by an empirical heat transfer coefficient. The corresponding energy flux

$$\dot{Q}_i = 4\pi r_s^2 \alpha_s (T_d - T_b) \tag{22}$$

describes the transfer from the interior of the droplet to its surface and contributes to the energy balance across the liquid–vapor interface:

$$\dot{Q}_i + \dot{m}_{\text{vap}} h_l(T_b) = \dot{m}_{\text{vap}} h(T_b) - 4\pi r^2 \lambda \frac{dT}{dr} = \dot{Q} \tag{23}$$

A schematic illustration of the model problem is given by Fig. 7, attributing the enthalpy of evaporation $\Delta h_v = h(T_b) - h_l(T_b)$ to the discontinuous change of enthalpy across the droplet surface. Equation (23) may be rearranged into an expression for the vapor mass flux:

$$\dot{m}_{\text{vap}} = \frac{\dot{Q}_i}{\Delta h_v} + \frac{1}{\Delta h_v} \left[4\pi r^2 \lambda \frac{dT}{dr} \right]_{r=r_s} \tag{24}$$

which can formally be decomposed into a contribution $\dot{m}_{\text{vap},c}$ due to heat conduction from the vapor phase and a contribution $\dot{m}_{\text{vap},f}$ due to energy transfer from the droplet interior:

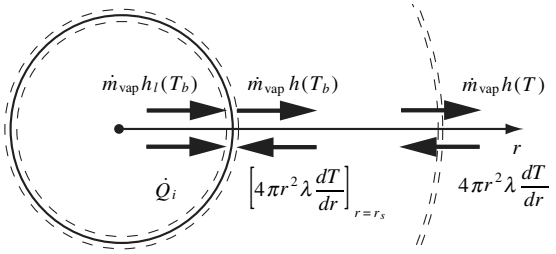

Fig. 7 Energy fluxes at the droplet surface and in the vapor phase.

$$\dot{m}_{\rm vap,c}=\frac{1}{\Delta h_v}\left[4\pi r^2\lambda\frac{dT}{dr}\right]_{r=r_s},\qquad \dot{m}_{{\rm vap},f}=\frac{4\pi r_s^2\alpha_s(T_d-T_b)}{\Delta h_v} \tag{25}$$

Eliminating $\dot{Q}$ by combining Eq. (19) and the corresponding boundary condition at the droplet surface given by the left-hand side of Eq. (23) and substituting $\dot{m}_{{\rm vap},f}\Delta h_v$ for $\dot{Q}_i$, an ordinary differential equation for the temperature in the vapor phase is obtained:

$$4\pi r^2\lambda\frac{dT}{dr}=\dot{m}_{\rm vap}c_p(T-T_b)+(\dot{m}_{\rm vap}-\dot{m}_{{\rm vap},f})\Delta h_v,\qquad r_s<r<\infty \tag{26}$$

To integrate this equation analytically, thermophysical properties are evaluated at a reference temperature and treated as constant according to the classical one-third rule [37]:

$$\lambda_{\rm ref}=\lambda(T_{\rm ref}),\qquad c_{p,{\rm ref}}=c_p(T_{\rm ref}),\qquad T_{\rm ref}=\tfrac{2}{3}T_b+\tfrac{1}{3}T_\infty \tag{27}$$

The final result is an implicit expression for $\dot{m}_{\rm vap}$ as a function of the Spalding heat transfer number B_T and the mass flux contribution $\dot{m}_{{\rm vap},f}$:

$$\dot{m}_{\rm vap}=2\pi r_s Nu^*\frac{\lambda_{\rm ref}}{c_{p,{\rm ref}}}\ell_n\left[1+\frac{B_T}{1-(\dot{m}_{{\rm vap},f}/\dot{m}_{\rm vap})}\right]$$
$$B_T=\frac{c_{p,{\rm ref}}(T_\infty-T_b)}{\Delta h_v} \tag{28}$$

The expression for classical D^2 theory [22] is recovered for the limit $\dot{m}_{{\rm vap},f}=0$. With respect to spray droplets moving in the vapor at a nonzero relative velocity, the energy transfer toward the surface is significantly increased due to forced convection. In the present framework, the classical Frössling correction [22] is employed to account for this effect:

$$Nu^*=2+0.552Re^{\frac{1}{2}}Pr^{\frac{1}{3}} \tag{29}$$

which is based on the following definitions of the Reynolds and Prandtl numbers:

$$Re=\frac{\rho_\infty c_{\rm rel}D}{\mu_{\rm ref}},\qquad Pr=\frac{\mu_{\rm ref}c_{p,{\rm ref}}}{\lambda_{\rm ref}} \tag{30}$$

The heat transfer coefficient α_s is specified by means of a correlation derived from spray evaporation measurements in internal combustion engines [38,39]:

$$\alpha_s=\begin{cases}760\Delta T^{0.26}, & 0\ {\rm K}\le\Delta T\le 5\ {\rm K}\\ 27\Delta T^{2.33}, & 5\ {\rm K}<\Delta T\le 25\ {\rm K}\\ 13800\Delta T^{0.39}, & 25\ {\rm K}<\Delta T\end{cases} \tag{31}$$

where $\Delta T=T_d-T_b$ is the superheat. As indicated in Fig. 8, a minimum value $\alpha_{s,\min}=2\lambda_l/D$, dependent on the droplet size, is used as an order-of-magnitude estimate to account for the effect of internal heat conduction. As a final result, the energy balance of the droplet is given by

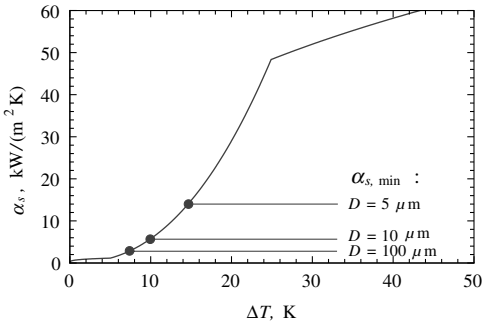

Fig. 8 Heat transfer coefficient.

$$\frac{dT_d}{dt}=\left[\dot{m}_{\rm vap}-4\pi r_s^2\frac{\alpha_s}{c_{p,l}}\right]\frac{T_d-T_b}{m_d} \tag{32}$$

Concluding, the model is used to analyze the flash evaporation dynamics of oxidizer droplets in an infinite quiescent-vapor atmosphere. Initial and boundary conditions are representative of engine preflow (compare Fig. 1): droplet initial temperature $T_{d,0}=292$ K, vapor temperature $T_\infty=269$ K, and pressure level $p_{\rm stat}=28$ kPa, resulting in a boiling temperature $T_b=268.7$ K (these data are taken from actual computations presented in Sec. III). Different initial droplet sizes are taken into account.

Figure 9 illustrates the results of simultaneous numerical integrations of Eqs. (21) and (32). It is apparent that the smaller droplets react significantly faster to the low-pressure environment. The temperature of the 25 μm droplet adapts to the boiling temperature within a few milliseconds, whereas the 150 μm droplet reacts much slower. Because $T_\infty\approx T_b$, the dominant driving force for heat and mass transfer is the superheat of the liquid and the droplet approaches a thermal equilibrium with the vapor phase. This asymptotic state of the droplet is determined by the energy balance (assuming a constant mean value $c_{p,l}$)

$$m_{d,0}c_{p,l}(T_{d,0}-T_b)=(m_{d,0}-m_d)\Delta h_v \tag{33}$$

and is independent of droplet size and thus reflects the global spray behavior. For the specified preflow conditions, only a small fraction of the injected liquid is actually evaporating, leading to a nondimensional mass loss $1-m_d/m_{d,0}=10.4\%$ and a corresponding nondimensional droplet diameter $D/D_0=95.3\%$.

E. Spray–Wall Interaction Model

Because of the limited evaporation, a considerable fraction of the spray impinges on the chamber walls. Because the time scales of droplet motion and flash evaporation are comparable, the majority of droplets are still superheated upon wall contact, and it has to be assumed that this affects the mechanism of interaction. A second important parameter is the surface temperature of the combustion chamber walls. For an isothermal initial state of the spacecraft, this temperature is initially equal to the injection temperature of the liquid. The first liquid entering the chamber vacuum is immediately vaporized, leading to a rapid pressure buildup. Reaching a certain

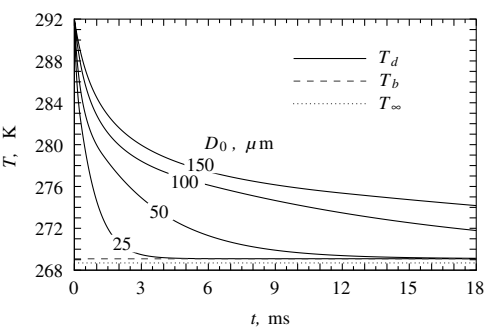

Fig. 9 Flash evaporation of N_2O_4 droplets.

pressure level, spray impinges on the chamber walls and the intense local heat and mass transfer rates result in a rapid drop of surface temperature. It seems plausible that the remaining superheat energy $m_d c_{p,l}(T_d - T_b)$ is converted immediately into vapor, with a certain contribution Q_w due to heat transfer from the wall.

The present modeling framework is based on droplet–wall interaction models derived in the frame of previous research on fuel preparation in a premix duct of an LPP combustor [10]. This framework is extended by accounting for the superheated state of the liquid and the potentially wide range of wall temperatures. The basic classification of the interaction mechanisms is illustrated in Fig. 10 using visualization data from literature [40–42]. Two different mechanism prevail at cold walls below the threshold temperature $T_w^* = 1.05T_b$: droplet deposition and droplet splashing, which is a partial deposition accompanied by an emission of secondary droplets. Quantification of the degree of deposition is based on an empirical correlation [43]

$$Re = 24SLa^{0.419} \tag{34}$$

relating the splashing parameter S to the values of the impact Reynolds number and the Laplace number:

$$Re = \frac{\rho_l c_n^* D}{\mu_l}, \qquad La = \frac{\rho_l \sigma D}{\mu_l^2} \tag{35}$$

where $c_n^* = c_d(\sin\alpha)^{0.63}$ represents a corrected normal velocity and α is the impact angle measured from the surface normal. The deposit mass fraction is then computed as $\eta = S^{-0.6}$, resulting in the following distribution of wall source terms:

$$S_{md}^w = \sum_{k=1}^{N} f_k \eta (m_d)_k \tag{36}$$

$$S_{\phi d}^w = \sum_{k=1}^{N} f_k \eta (m_d \phi_d)_k, \qquad \phi = u, v, w, h \tag{37}$$

The emission of small secondary droplets is modeled as a stochastic process, similar to the presented primary atomization model. A log-normal distribution is used to describe the diameter of the droplets, along with distributions for injection position and velocity. Droplet splashing on the cylindrical chamber surface close to the injectors is depicted in Fig. 11. As discussed previously, the superheat of droplets is converted instantaneously into vapor and the remaining deposit assumes the local boiling temperature.

Droplet impact on hot walls results in either nucleate boiling of the deposit (below a modified Leidenfrost temperature T_L^*) or in reflection of the droplet (above T_L^*). Nucleate boiling on hot walls is idealized as an immediate evaporation of the impinging droplet by heat transfer from the wall. The modified Leidenfrost temperature is calculated from [10]

$$\frac{T_L^* - T_L}{T_L} = 0.027\sqrt{We_d} \tag{38}$$

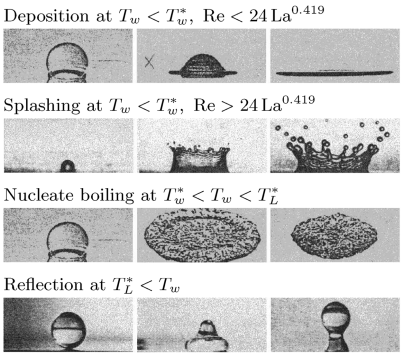

Fig. 10 Droplet–wall interaction mechanisms [10] (images from [40–42].

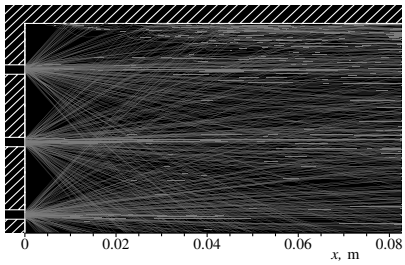

Fig. 11 Droplet splashing on chamber wall at $T_w \approx T_b$.

where $We_d = \rho_d (c_n^*)^2 D/\sigma$ denotes the impact Weber number and $T_L = 1.2T_b$ is an approximation of the Leidenfrost temperature. The reflection model for impact above T_L^* is based on an empirical damping correlation.

As described, the wall surface experiences a significant temperature drop during preflow. However, experimental data on transient temperature and heat flux distributions are generally unavailable, and a conjugate heat transfer analysis is out of the scope of the present study. For this reason, the effect on the preflow has been assessed by investigating the two physical limiting cases of isothermal ($T_w = T_{\mathrm{inj}}$) and adiabatic ($Q_w = 0$) wall boundary conditions.

For the investigated range of preflow conditions, isothermal wall conditions lead to nucleate boiling and complete evaporation of impinging droplets. In this case, the major fraction of the energy is provided as a wall heat flux formally expressed as $Q_w \gg m_d c_{p,l}(T_d - T_b)$. For adiabatic conditions, the partial evaporation at the wall is driven solely by the internal energy of the impacting droplet. This is an idealization of the case $Q_w \ll m_d c_{p,l}(T_d - T_b)$ and results in wall surface temperatures close to the local boiling temperature. Based on the experimental chamber pressure and temperature data presented in the following section, it can be concluded that adiabatic wall conditions prevail during the preflow phase.

III. Results

The results presented in the following sections describe the oxidizer preflow during startup of the Aestus upper-stage engine. Because the injector arrangement on the base plate is symmetric with respect to an axis-aligned plane, it is assumed that the generated two-phase flowfield is symmetric and that it is thus sufficient to consider only a 180 deg section of the flow domain. Note that the result plots illustrate only a part of the computational domain and that the supersonic outlet boundary is not included.

A. Stationary Two-Phase Flowfield

The flowfield is illustrated in Fig. 12 by longitudinal sections perpendicular to the symmetry plane for three initial droplet size spectra and a constant liquid injection temperature. Contour plots of the vapor temperature are arranged in the left column, and the right column contains the corresponding plots of the Sauter mean diameter of the polydisperse liquid phase. It is obvious that the vapor temperature is nearly uniform in the combustion chamber, decreasing drastically in the expanding nozzle flow. As a significant difference from single-phase nozzle flow, the Mach lines indicate an extension of the subsonic core flow region into the divergent part of the nozzle, an effect that is particularly pronounced for the fine spray ($D_{63,0} = 50\ \mu$m). On the other hand, the coarser sprays ($D_{63,0} = 100$ and $150\ \mu$m) show a distinct region of elevated vapor temperature along the divergent nozzle contour.

As will be seen in the subsequent analysis, this is mainly a consequence of droplet impact and splashing on the chamber wall toward the nozzle throat, generating a large number of small secondary droplets. This mechanism is reflected in the markedly low value of D_{32} in this region, as indicated by the $D_{32} = 30\ \mu$m isolines. Because of the small size of these droplets, they are easily dragged with the flow along the nozzle contour, where they increase the

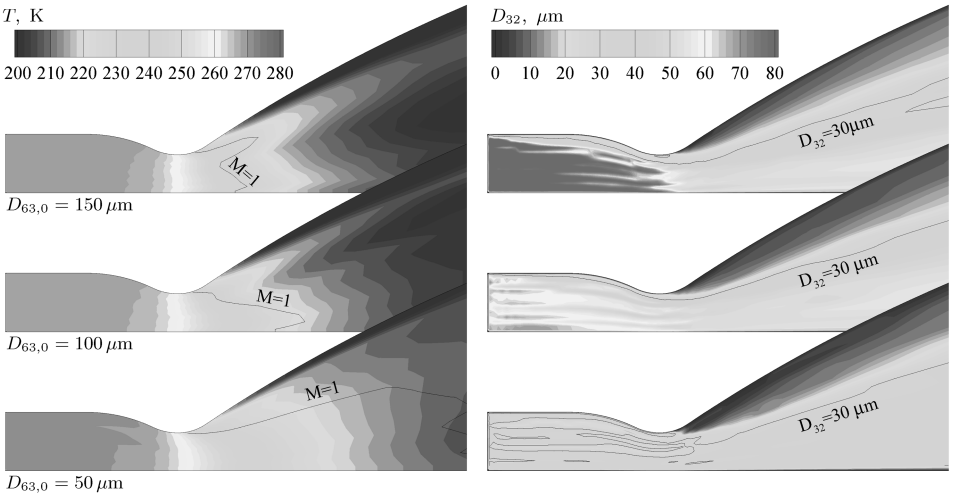

Fig. 12 Longitudinal sections of the two-phase flowfield for $T_{inj} = 292$ K.

temperature of the vapor flow by rapid flash evaporation. All three cases are characterized by streaks of increased D_{32}, which is an obvious consequence of the finite number of injection elements and the dense core structure of the plain-orifice sprays. Throughout the combustion chamber, the dispersion of the spray droplets perpendicular to the axis is less pronounced than the axial propagation of the spray.

More detailed information on the evaporation dynamics is gained from a single-droplet analysis. Based on the preceding flowfields for three different initial droplet size spectra, Fig. 13 comprises trajectory data of single droplets injected with the mean size $D_0 = D_{63,0}$ and moving roughly along the chamber axis. Because the 150 μm droplet is destroyed by the increased aerodynamic forces in the throat region, the trajectory data of a representative secondary droplet are appended.

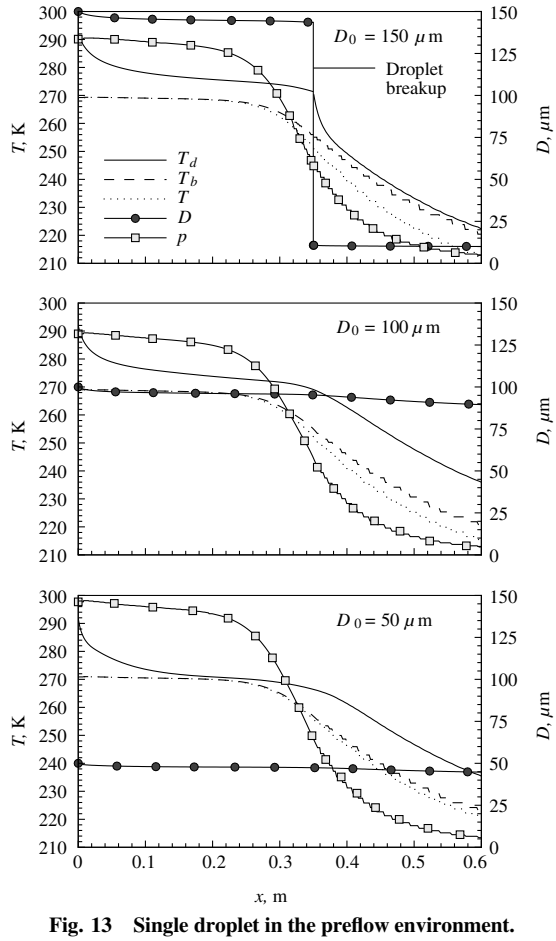

Fig. 13 Single droplet in the preflow environment.

In general, the temperature of the smaller droplets drops faster to the local boiling temperature, which is at a nearly constant level in the combustion chamber and decreases with the static pressure in the accelerated nozzle flow (the pressure in Fig. 13 ranges from 0 to 32 kPa). As remarked in the context of Fig. 9, the maximum reduction of droplet sizes in the combustion chamber is about 5%. In all three cases, the droplets leaving the combustion chamber are still superheated. The decrease of the boiling temperature in the nozzle flow leads to a second phase of flash evaporation. Closely linked to the evaporation dynamics is the decrease of vapor temperature in the nozzle flow. In the axis region, this decrease is less pronounced for the fine spray, because mass and energy release from smaller droplets proceeds on a shorter time scale. Along the divergent nozzle contour, the same mechanism is responsible for the increased vapor temperature for the coarser sprays, due to small secondary droplets generated by splashing, as already explained in the context of Fig. 12.

A three-dimensional representation of the Sauter mean diameter is given in Fig. 14 for the computational base case of $T_{inj} = 292$ K and $D_{63,0} = 100$ μm. The distribution indicates a significant inhomogeneity of the dispersed phase throughout the combustion chamber, in which the cross-sectional pattern is closely associated with the injector arrangement on the base plate. Corresponding to Fig. 12, the Mach surface reaches far into the divergent part, in which it exhibits considerable asymmetry.

A second parametric study is dedicated to the influence of the injection temperature on the preflow. To characterize the thermodynamic state of the vapor phase in the combustion chamber, the temperature T_{stat} and pressure p_{stat} are chosen at specific measurement locations close to the base plate. Figure 15 depicts the continuous increase of T_{stat} for increasing injection temperature, both for adiabatic ($T_w \approx T_{stat}$) and for isothermal ($T_w \approx T_{inj}$) wall

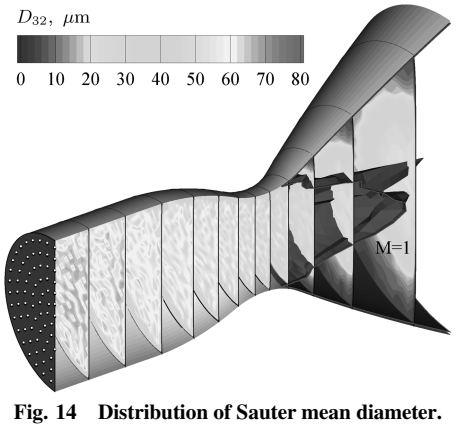

Fig. 14 Distribution of Sauter mean diameter.

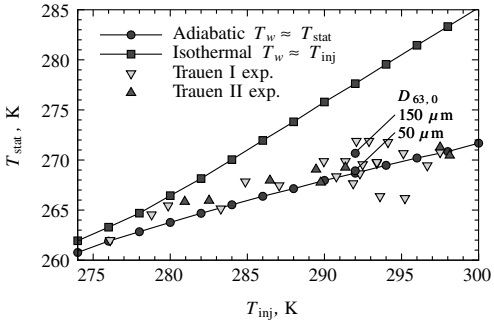

Fig. 15 Effect of injection temperature ($D_{63,0} = 100$ μm).

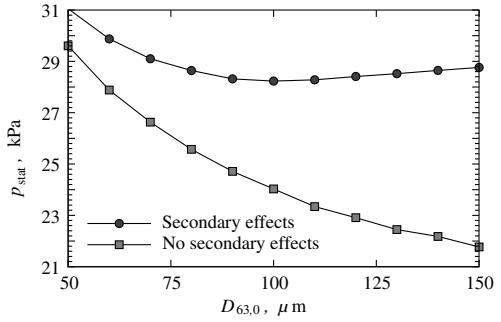

Fig. 18 Pressure in the combustion chamber ($T_{inj} = 292$ K).

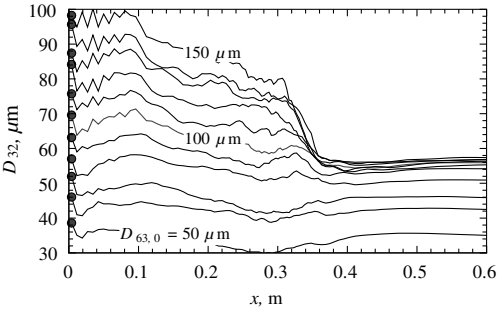

Fig. 19 Sauter mean diameter along the axis.

conditions. At $T_{inj} = 292$ K, the additional effect of the initial droplet size spectrum is indicated for two extreme deviations from the base value of $D_{63,0} = 100$ μm. Also included are data of the Trauen I and II test series. The comparison of computed and experimental data supports the initial assumption that adiabatic wall conditions are the appropriate boundary conditions for the preflow regime. For increased injection temperatures, isothermal wall conditions result in unrealistically high temperature and pressure levels in the combustion chamber. The underlying reasons for this behavior are nucleate boiling and droplet destruction on hot walls. In Fig. 16, the nearly isobaric drop from the liquid injection temperature T_{inj} to the vapor temperature $T_{stat} \approx T_b$ in the chamber is depicted (compare Fig. 1). Although the temperature of the flash-evaporating droplets is monotonously decreasing, it is not actually reaching the equilibrium boiling state in the chamber, due to the limited residence time.

A similar representation is chosen to illustrate the effect of varying initial droplet size spectra. Figures 17 and 18 depict the evolutions of vapor temperature and chamber pressure for the computed range of $D_{63,0}$. In addition, Fig. 19 shows the corresponding evolutions of the Sauter mean diameter of the spray along the axis. For the finer sprays ($D_{63,0} \leq 90$ μm), the decrease of temperature and pressure with increasing size spectra is a consequence of the longer time scales of flash evaporation from larger droplets. However, for the coarser sprays ($D_{63,0} \geq 110$ μm), temperature and pressure are again increasing with increasing size spectra, an effect that is due to the increasing generation of secondary droplets by droplets splashing on the convergent chamber wall and aerodynamic droplet breakup in the throat. The latter is obvious from Fig. 19, showing a distinct decrease of D_{32} in the throat region for $D_{63,0} > 100$ μm. Consequently, Figs. 17 and 18 indicate a minimum temperature and pressure for $D_{63,0} = 100$ μm. If no secondary breakup is taken into account, T_{stat} and p_{stat} are decreasing monotonously.

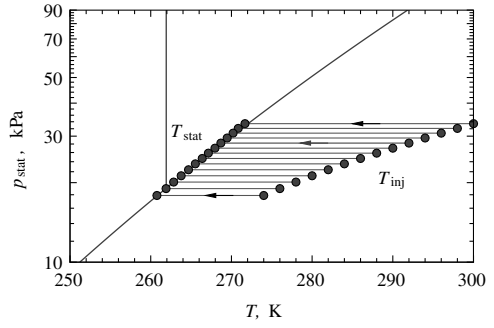

Fig. 16 Temperature drop in chamber ($D_{63,0} = 100$ μm).

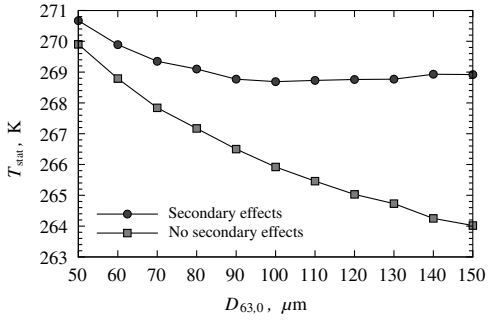

Fig. 17 Temperature in the combustion chamber ($T_{inj} = 292$ K).

B. Spray Deposition

Spray deposition on the inner surface of the combustion chamber is characterized by a bimodal character. As illustrated in Figs. 20 and

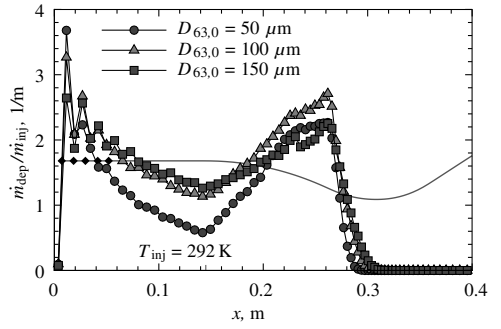

Fig. 20 Spray deposit density for varying $D_{63,0}$.

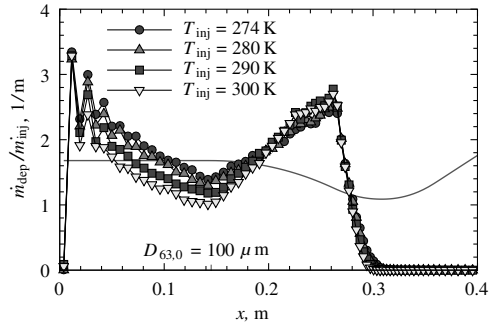

Fig. 21 Spray deposit density for varying T_{inj}.

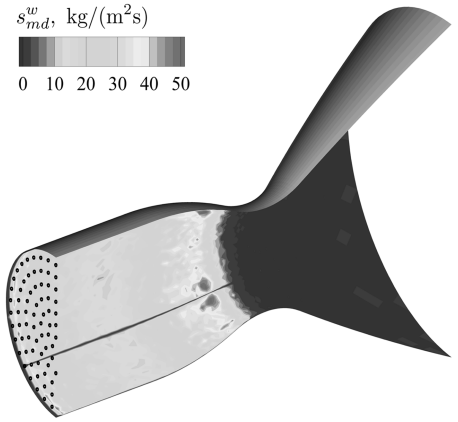

Fig. 22 Spray deposit density.

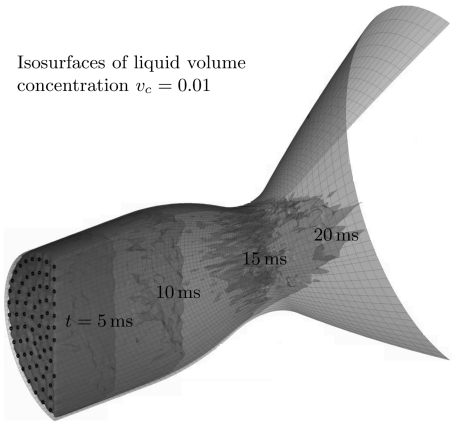

Fig. 23 Evolution of the spray front surface.

21, the normalized axial deposition density $\dot{m}_{\text{dep}}/\dot{m}_{\text{inj}}$ is highest on the cylindrical part close to the base plate and decreases with increasing distance from the base plate. This massive oxidizer deposition is potentially dangerous, because it may lead to considerable accumulation of liquid and uncontrolled effects on the ignition phase, particularly when acoustic cavities are present. A second maximum of the deposition density occurs on the converging part of the nozzle toward the throat. The first maximum close to the base plate is a consequence of the wide-angle flash atomization of the injected liquid and contrasts the behavior at nominal operation of the engine [44]. Because of the positioning of the injectors on discrete coaxial rings, the deposition density shows considerable fluctuations in the vicinity of the base plate. This explanation is also evident from the inhomogeneity of the spray impingement pattern illustrated in Fig. 10 and from the deposition density s^w_{md} depicted in Fig. 22 for $T_{\text{inj}} = 292$ K and $D_{63,0} = 100$ μm.

Close to the base plate, the deposition density is increasing with decreasing droplet size, which is a direct consequence of the empirical correlations describing droplet–wall interaction. With increasing distance from the base plate, aerodynamic drag forces deflect the small droplets of the spray toward the nozzle throat. Consequently, the coarse fraction of the spray increases and the deposition decreases. This aerodynamic mechanism is also dominant throughout the combustion chamber for the coarser sprays ($D_{63,0} \geq 110$ μm), which are subject to secondary-droplet breakup (compare Fig. 19). Again, the small secondary droplets generated in the converging part of the nozzle are deflected in the flow direction, preventing wall impact.

With respect to Fig. 20, this effect is evident from the less distinctive rise of the deposition density for the coarse spray ($D_{63,0} = 150$ μm). Maximum deposition occurs for $D_{63,0}=$ 100 μm, because this is the coarsest spray that is unaffected by secondary breakup, as evident from Fig. 19. For increasing injection temperature, the deposition density on the cylindrical part of the chamber surface decreases. This effect is caused by increased evaporation of droplets and inverses in the converging part, because the reduced size of the droplets increases the deposition rate. Accumulation on the base plate could not be assessed in the present study, due to the limited resolution of the computational grid, which does not allow for capturing of small-scale recirculation zones and hence the possible entrainment and deposition of droplets.

C. Dynamic Spray Analysis

Based on the steady-state two-phase flowfield, a dynamic spray analysis is performed. The propagation of the liquid volume concentration is shown in Fig. 23 by four representative time levels. The typical total duration of an engine preflow is about $\Delta t_0 \approx$ 200 ms, which is 1 order of magnitude longer than the depicted time frame. The temporal evolution of the vapor generation in the combustion chamber is of major importance for the analysis of highly transient processes such as engine ignition and combustion. To cast the computational results of the present study into a modeling frame suitable to system-analysis tools [3–5], the integral vapor generation is described by transfer functions.

Figures 24 and 25 illustrate these functions for varying injection temperature and for varying initial droplet size spectra. The sudden increase of the vapor mass flow rate at $t \approx 15$ ms is a result of the spray passing the nozzle throat and thus being exposed to a severe drop of the flow pressure (compare Fig. 23). With respect to the indicated maximum value of $\dot{m}_{\text{vap}}/\dot{m}_{\text{inj}} = 10.4\%$ ($t < 15$ ms), which is valid for an injection temperature of $T_{\text{inj}} = 292$ K, it is evident that the two-phase flow reaching the nozzle throat at $t \approx 15$ ms is not in thermal equilibrium.

An evaluation of the transfer function in the divergent part of the nozzle is depicted in Fig. 26. It confirms that the minimum chamber pressure reached for the $D_{63,0} = 100$ μm spray coincides with a minimum rate of evaporation in the expansion nozzle. This minimum rate has been explained as a coupled effect of secondary-droplet breakup and spray–wall interaction, which mainly affects the coarser sprays ($D_{63,0} \geq 110$ μm) and intensifies the evaporation of the spray past the throat.

Summarizing, it can be stated that the variation of the injection temperature has the most distinctive effect by basically shifting the

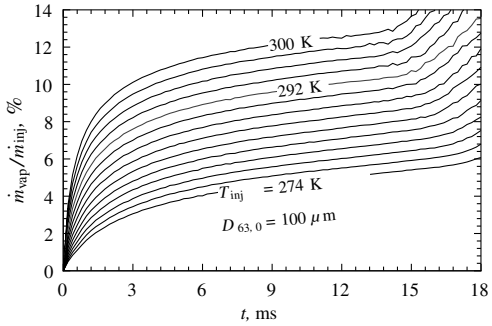

Fig. 24 Effect of injection temperature on the transfer function.

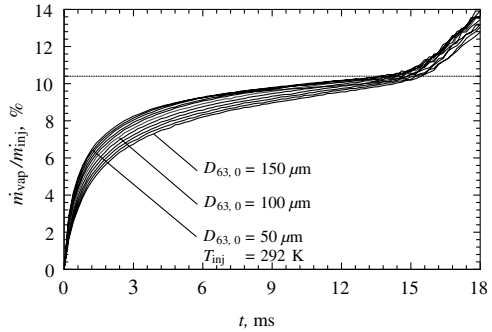

Fig. 25 Effect of size distribution on the transfer function.

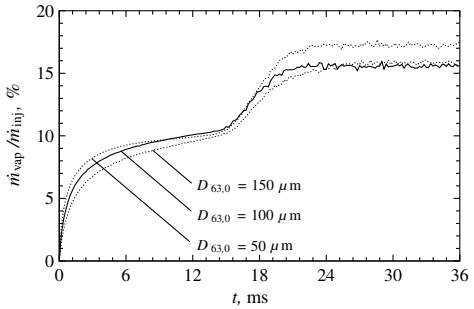

Fig. 26 Evaporation in the nozzle extension.

level of the transfer function. Variation of the initial size spectra, on the other hand, has a predominant influence on the *slope* of the transfer function in the combustion chamber.

IV. Conclusions

In contrast to nominal operation, the low-pressure preflow in an upper-stage rocket engine is characterized by flash evaporation of superheated liquid oxidizer. The objective of the presented computational analysis is a refined understanding and modeling of the phenomena during preflow as a contribution for an accurate system-level description of the engine startup behavior. Based on an iterative Euler–Lagrange method, particular importance is attributed to the dynamics of the flash evaporation process and to secondary effects such as aerodynamic droplet breakup and droplet–wall interaction. The polydisperse character of the spray is taken into account by an empirical flash atomization model.

Because of the finite time scale of flash evaporation, the dispersed liquid phase is in a permanent state of superheat, ranging from combustion chamber to nozzle exit. Consequently, an assumption of local thermodynamic equilibrium would significantly overestimate the degree of evaporation. The analysis indicates that pressure and temperature levels in the chamber are controlled by many factors. Basically, the levels increase with increasing injection temperature of the liquid and increasing wall temperature, but decrease with the initial droplet size spectrum of the spray.

A decisive effect of aerodynamic droplet breakup and droplet–wall interaction is apparent for coarser sprays that counteracts the effect of the initial droplet size spectrum by the generation of small secondary droplets. Thus, minimum pressure and temperature levels are reached for an initial size spectrum of $D_{63,0} = 100$ μm, assuming a Rosin–Rammler distribution with $n = 2.4$. This minimum corresponds to a maximum viable mean size of droplets in the combustion chamber. Hence, the evaporation rate is smallest, resulting in the lowest levels of pressure and temperature.

Furthermore, the typical wide-angle character from flash atomization causes massive liquid deposition on the cylindrical part of the combustion chamber. The distribution is characterized by a bimodal behavior. The first maximum of the deposition rate is located next to the base plate, and the second maximum occurs on the convergent part of the throat. The analysis is applicable to bipropellant systems and to other technical flow processes involving flash evaporation at low-pressure conditions. The computational approach has been further substantiated and refined in several other studies of experimental and computational nature [33,45].

Acknowledgments

The authors acknowledge the interest and support of ESA for this research activity, which has been conducted in the frame of an internal research fellowship. They appreciate the provision of measurement data from the Aestus engine tests that were performed by DLR Lampoldshausen on the Trauen test site using hardware designed by Astrium Space Transportation under the management of the Centre National d'Etudes Spatiales (CNES Evry). They also appreciate the related fruitful discussions with M. Oschwald, O. de Bonn, and M. Delanoue.

References

[1] Boorady, F. A., and Douglass, D. A., "Solution of the High-Vacuum Hard-Start Problem of the IRFNA-UDMA Rocket for Gemini Agenda," *Journal of Spacecraft and Rockets*, Vol. 5, No. 1, 1968, pp. 22–30. doi:10.2514/3.29180

[2] Dadieu, A., Damm, R., and Schmidt, E. W., *Raketentreibstoffe*, Springer, New York, 1968.

[3] Keppeler, J., Boronine, E., and Fassl, F., "Startup Simulation of Upper Stage Propulsion System of Ariane 5," *4th International Conference on Launcher Technology "Space Launcher Liquid Propulsion"* [CD-ROM], Centre National d'Etudes Spatiales, Paris, 2002.

[4] Legrand, B., Albano, G., and Vuillermoz, P., "Start Up Transient Modelling of Pressurized Tank Engine: Aestus Application," *4th International Conference on Launcher Technology "Space Launcher Liquid Propulsion"* [CD-ROM], Centre National d'Etudes Spatiales, Paris, 2002.

[5] Ordonneau, G., Albano, G., and Masse, J., "CARINS: A Future Versatile and Flexible Tool for Engine Transient Prediction," *4th International Conference on Launcher Technology "Space Launcher Liquid Propulsion"* [CD-ROM], Centre National d'Etudes Spatiales, Paris, 2002.

[6] Steelant, J., "Fluid Dynamic Effects During Priming of Aestus' Fuel Dome," *European Journal of Mechanical*, Vol. 48, No. 2, 2003, pp. 93–100.

[7] Dutheil, J. P., and Langel, G., "Ariane 5 Upper-Stage Ignition Conditions Improvement, and Return to Operation with ENVISAT Payload," *Astronautica Acta*, Vol. 53, No. 4, 2003, pp. 585–595. doi:10.1016/S0094-5765(03)80020-6

[8] Schmehl, R., and Steelant, J., "Flash Evaporation of Oxidizer Spray During Start-Up of an Upper-Stage Rocket Engine," AIAA Paper 2003-5075, 2003.

[9] Schmehl, R., and Steelant, J., "Influence of Injection Temperature on the Preflow Phase During Start-Up of an Upper-Stage Rocket Engine," AIAA Paper 2004-4011, 2004.

[10] Schmehl, R., Rosskamp, H., Willmann, M., and Wittig, S., "CFD Analysis of Spray Propagation and Evaporation Including Wall Film Formation and Spray/Film," *International Journal of Heat and Fluid Flow*, Vol. 20, No. 5, 1999, pp. 520–529. doi:10.1016/S0142-727X(99)00041-7

[11] Schmehl, R., Maier, G., and Wittig, S., "CFD Analysis of Fuel Atomization, Secondary Droplet Breakup and Spray Dispersion in the Premix Duct of a LPP Combustor," *8th International Conference on Liquid Atomization and Spray Systems (ICLASS 2000)* [CD-ROM], ILASS-Europe, 2000.

[12] Schmehl, R., "Deformation and Breakup of Liquid Droplets in Technical Mixture Preparation Processes," Ph.D. Dissertation, Univ. of Karlsruhe, Karlsruhe, Germany, 2003 (in German).

[13] Crowe, C. T., "Review—Numerical Models for Dilute Gas-Particle Flows," *Journal of Fluids Engineering*, Vol. 104, Sept. 1982, pp. 297–303.

[14] Wittig, S., Hallmann, M., Scheurlen, M., and Schmehl, R., "A New Eulerian Model for Turbulent Evaporating Sprays in Recirculating Flows," AGARD Paper CP-536, 1993, pp. 37.1–37.11.

[15] Preclik, D., Estublier, D., and Wennerberg, D., "An Eulerian-Lagrangian Approach to Spray Combustion Modeling for Liquid Bi-Propellant Rocket Motors," AIAA Paper 95-2779, 1995.

[16] Schmehl, R., Klose, G., Maier, G., and Wittig, S., "Efficient Numerical Calculation of Evaporating Sprays in Combustion Chamber Flows," Research and Technology Organisation Paper MP-14, 1998, pp. 51.1–51.13.

[17] Burger, M., Klose, G., Rottenkolber, G., Schmehl, R., Giebert, D., Schäfer, O., Koch, R., and Wittig, S., "Combined Eulerian and Lagrangian Method for Prediction of Evaporating Sprays," *Journal of Engineering for Gas Turbines and Power*, Vol. 124, No. 3, 2002, pp. 481–488. doi:10.1115/1.1473153

[18] Faeth, G. M., "Evaporation and Combustion of Sprays," *Progress in Energy and Combustion Science*, Vol. 9, Pergamon, New York, 1983, pp. 1–76. doi:10.1016/0360-1285(83)90005-9

[19] Karki, K., and Patankar, S., "Pressure Based Calculation Procedure for Viscous Flows at All Speeds in Arbitrary Configurations," *AIAA Journal*, Vol. 27, No. 9, 1989, pp. 1167–1174. doi:10.2514/3.10242

[20] Noll, B., "Evaluation of a Bounded High-Resolution Scheme for Combustor Flow Computations," *AIAA Journal*, Vol. 30, No. 1, 1992, pp. 64–69. doi:10.2514/3.10883

[21] Crowe, C. T., Sharma, M. P., and Stock, D. E., "The Particle-Source-in-Cell (PSI-CELL) Model for Gas-Droplet Flows," *Journal of Fluids Engineering*, Vol. 99, June 1977, pp. 325–332.

[22] Aggarwal, S. K., and Peng, F., "A Review of Droplet Dynamics and Vaporization Modeling for Engineering Calculations," *Journal of Engineering for Gas Turbines and Power*, Vol. 117, No. 3, 1995, pp. 453–461. doi:10.1115/1.2814117

[23] Wiegand, H., "The Effect of a Uniform Flowfield on Freely Moving Droplets and Their Drag Coefficient in the Reynolds Number Range of 50 to 2000," *Fortschrittberichte VDI*, Vol. 7, No. 120, 1987 (in German).

[24] Schmehl, R., "Advanced Modelling of Droplet Deformation and Breakup for CFD Analysis of Mixture Preparation," *18th Annual Conference on Liquid Atomization and Spray Systems (ILASS-2002)* [CD-ROM], ILASS-Europe, 2002.

[25] Gosman, A. D., and Ioannides, E., "Aspects of Computer Simulation of Liquid-Fueled Combustors," *Journal of Energy*, Vol. 7, No. 6, 1983, pp. 482–490. doi:10.2514/3.62687

[26] Patankar, S. V., *Numerical Heat Transfer and Fluid Flow*, McGraw–Hill, New York, 1980.

[27] Merci, B., Steelant, J., Vierendeels, J., Riemslagh, K., and Dick, E., "Computational Treatment of Source Terms in Two-Equation Turbulence Models," *AIAA Journal*, Vol. 38, No. 11, 2000, pp. 2085–2093. doi:10.2514/2.870

[28] Kohnen, G., Rüger, M., and Sommerfeld, M., "Convergence Behaviour for Numerical Calculations by the Euler/Lagrange Method for Strongly Coupled Phases," *Numerical Methods in Multiphase Flows*, Vol. 185, American Society of Mechanics Engineers, Fluids Engineer Div., New York, 1994, pp. 27–32.

[29] Burger, M., Schmehl, R., Koch, R., Wittig, S., and Bauer, H.-J., "DNS Study of Droplet-Vortex Interaction in a Karman Vortex Street," *International Journal of Heat and Fluid Flow*, Vol. 27, No. 2, 2006, pp. 181–191. doi:10.1016/j.ijheatfluidflow.2005.09.004

[30] Pouvreau, L., Yoshizaki, T., and Nishida, K., "Atomization of a Heated Liquid Jet: Enhancement of Breakup and Dispersion Through a Hole Nozzle," *8th International Conference on Liquid Atomization and Spray Systems (ICLASS 2000)* [CD-ROM], ILASS-Europe, 2000.

[31] Lecourt, R., and d'Herbigny, F. X., "MMH/NTO Injection and Ignition in Vacuum Downstream from an Aestus Single Injection Element," *Aerospace Science and Technology*, Vol. 8, No. 3, 2004, pp. 207–217. doi:10.1016/j.ast.2003.11.001

[32] Hervieu, E., and Veneau, T., "Experimental Determination of the Droplet Size and Velocity Distributions at the Exit of the Bottom Discharge Pipe of a Liquefied Propane Storage Tank During a Sudden Blowdown," *Journal of Loss Prevention in the Process Industries*, Vol. 9, No. 6, 1996, pp. 413–425. doi:10.1016/S0950-4230(96)00030-7

[33] Lecourt, R., Barricau, P., and Steelant, J., "Spray Velocity and Drop Size Measurements in Vacuum Conditions," *Atomization and Sprays*, Vol. 19, No. 2, 2009, pp. 103–133. doi:10.1615/AtomizSpr.v19.i2.10

[34] Lefebvre, A. H., *Atomization and Sprays*, Hemisphere, New York, 1998.

[35] Park, B. S., and Lee, S. Y., "An Experimental Investigation of the Flash Atomization Mechanism," *Atomization and Sprays*, Vol. 4, No. 2, 1994, pp. 159–179.

[36] Sirignano, W. A., *Fluid Dynamics and Transport of Droplets and Sprays*, Cambridge Univ. Press, New York, 1999.

[37] Sparrow, E. M., and Gregg, J. L., "The Variable Fluid Property Problem in Free Convection," *Transactions of the ASME*, Vol. 80, 1958, pp. 879–886.

[38] Adachi, M., McDonell, V. G., Tanaka, D., Senda, J., and Fujimoto, H., "Characterization of Fuel Vapor Concentration Inside a Flash Boiling Spray," Society of Automotive Engineers Paper 970871, 1997.

[39] Zuo, B., Gomes, A., and Rutland, C. J., "Modeling Superheated Fuel Sprays and Vaporization," *International Journal of Engine Research*, Vol. 1, No. 4, 2000, pp. 321–336. doi:10.1243/1468087001545218

[40] Chandra, S., and Avedisian, C., "On the Collision of a Droplet with a Solid Surface," *Proceedings of the Royal Society of London A*, Vol. 432, No. 1884, 1991, pp. 13–41. doi:10.1098/rspa.1991.0002

[41] Macklin, W., and Metaxas, G., "Splashing of Drops on Liquid Layers," *Journal of Applied Physics*, Vol. 47, No. 9, 1976, pp. 3963–3970. doi:10.1063/1.323218

[42] Wachters, L., and Westerling, N., "The Heat Transfer from a Hot Wall to Impinging Water Drops in the Spheroidal State," *Chemical Engineering Science*, Vol. 21, No. 11, 1966, pp. 1047–1056. doi:10.1016/0009-2509(66)85100-X

[43] Samenfink, W., Elsäßer, A., Dullenkopf, K., and Wittig, S., "Droplet Interaction with Shear Driven Liquid Films: High Quality Measurements of the Deposited Mass Fraction," *13th Annual Conference on Liquid Atomization and Spray Systems (ILASS-Europe'97)*, ILASS-Europe, 1997, pp. 480–486.

[44] Knab, O., Fröhlich, A., and Wennerberg, D., "Design Support for Advanced Storable Propellant Engines by ROCFLAM Analyses," AIAA Paper 99-2459, 1999.

[45] Raju, M. S., "CFD Modeling of Superheated Fuel Spray," AIAA Paper 2009-1187, 2009.

D. Talley
Associate Editor